

Morphology of the Secondary CMB Anisotropies: the Key to “Smoldering” Reionization

Nickolay Y. Gnedin¹ and Sergei F. Shandarin²

¹*Center for Astrophysics and Space Astronomy, University of Colorado, Boulder, CO 80309, USA; gnedin@casa.colorado.edu*

²*Department of Physics and Astronomy, University of Kansas, Lawrence, KS 66045, USA; sergei@ku.edu*

ABSTRACT

We show how the morphological analysis of the maps of the secondary CMB anisotropies can detect an extended period of “smoldering” reionization, during which the universe remains partially ionized. Neither radio observations of the redshifted 21cm line nor IR observations of the redshifted Lyman-alpha forest will be able to detect such a period. The most sensitive to this kind of non-gaussianity parameters are the number of regions in the excursion set, N_{cl} , the perimeter of the excursion set, P_g , and the genus (i.e. '1 - number of holes') of the largest (by area) region. For example, if the universe reionized fully at $z = 6$, but maintained about 1/3 mean ionized fraction since $z = 20$, then a 2 arcmin map with 500^2 pixel resolution and a signal-to-noise ratio $S/N = 1/2$ allows to detect the non-gaussianity due to reionization with better than 99% confidence level.

Key words: cosmic microwave background - cosmology: theory - cosmology: large-scale structure of universe - galaxies: formation - galaxies: intergalactic medium

1 INTRODUCTION

Recent observations of high redshift quasars (Becker et al. 2001; Djorgovski et al. 2001) offer a unique probe of the physical conditions in the intergalactic medium (IGM) shortly after the epoch of reionization. Similar future observations will increase the amount of observational data multi-fold and will provide critical constraints on the theories of galaxy formation.

However, if we want to go beyond the epoch of reionization and to study the pre-overlap stage during which ionized H II regions expand into still neutral low density gas, we need to use different bands of electromagnetic spectrum. Next Generation Space Telescope (NGST) will provide valuable clues on the earliest episodes of galaxy formation from infra-red observations, although a relationship between the first galaxies and the properties of the IGM at high redshifts will not necessarily be easy to determine from such observations. Radio observations of the redshifted 21 cm line of neutral hydrogen might be capable of measuring the pre-reionization signal (Madau, Meiksin, & Rees 1997; Tozzi et al. 2000; Iliev et al. 2002; Carilli, Gnedin, & Owen 2002), although such a measurement will be at the very edge of the capability of the next generation radio instruments such as Low Frequency Array (LOFAR).

Another possible channel to probe the pre-overlap stage of reionization is studying secondary CMB anisotropies (Hu & White 1996; Aghanim et al. 1996; Knox, Scoccimarro, & Dodelson 1998; Gruzinov & Hu 1998; Jaffe & Kamionkowski

1998; Peebles & Juszkievicz 1998; Haiman & Knox 1999; Hu 2000; Bruscoli et al. 2000; da Silva et al. 2000; Refregier et al. 2000; Springel, White, & Hernquist 2001; Seljak, Burwell, & Pen 2001; Gnedin & Jaffe 2001). While such a measurement is also in the future, observations of the secondary CMB anisotropies can provide constraints on the physical conditions in the IGM that are not accessible by other means. In fact, because CMB anisotropies are sensitive to the total Thompson optical depth, they can probe low levels of ionization in the mostly neutral gas - which cannot be done by radio observations of the redshifted 21 cm line.

Several scenarios have been proposed recently in which the universe undergoes a protracted episode of incomplete ionization prior to full reionization, either due to early supernova-driven winds (Madau, Ferrara, & Rees 2001; Oh et al. 2001) or ionizations by energetic X-rays (Oh 2001; Venkatesan, Giroux, & Shull 2001). This kind of “smoldering” reionization (which results in a partial reduction in the neutral hydrogen fraction) will be virtually impossible to detect with radio observations. Such a signature also cannot be detected by measuring just the spectrum of the fluctuations, because, as was shown in Gnedin & Jaffe (2001), the power spectrum of secondary anisotropies is only weakly dependent on the redshift of reionization. However, Gnedin & Jaffe (2001) noticed that the fluctuations themselves were highly non-gaussian. In this paper we show how tests of the non-gaussianity of the secondary CMB anisotropies can detect the signature of an epoch of “smoldering reionization”.

The physical reason behind such a possibility is simple:

the earlier the epoch of “smoldering reionization” begins, the more nonlinear the objects that are responsible for the production of ionizing photons should be, and, therefore, the more non-gaussian the secondary CMB anisotropies will be. And it does not matter for this test what the sources of ionizations really are, only that they form early and, therefore, highly nonlinear at early times, when the linear fluctuations are smaller.

A big advantage of a morphological approach is that it is virtually independent of assumptions about the underlying cosmological model. For example, the redshifted 21cm emission and absorption will depend on the rate at which ionization front expand into the low density IGM, gobbling up the neutral gas on the way. And because secondary CMB anisotropies are dominated by nonlinear structures on small scales (Gnedin & Jaffe 2001), they are insensitive to the specific details of how ionization fronts expand.

2 METHOD

2.1 Simulations

In this paper we use the synthetic maps of the secondary CMB anisotropies from Gnedin & Jaffe (2001). These maps were obtained from a numerical simulation of cosmological reionization, published in Gnedin (2000).

The simulation included all the physical ingredients required to study the process of reionization, including the 3D radiative transfer. It assumed a currently fashionable CDM+ Λ cosmological model with $\Omega_{m,0} = 0.3$, $\Omega_{\Lambda,0} = 0.7$, $h = 0.7$, $\Omega_{b,0} = 0.04$, $n = 1$, $\sigma_8 = 0.91$ in a comoving box with the size of $4h^{-1}$ Mpc. However, for the purpose of this paper the specific details about a cosmological model are unimportant.

For the considered cosmology the angular size of a fixed comoving length is almost independent of redshift for $z \sim 10$. For example, our $4h^{-1}$ Mpc box subtends 2.7 arcmin at $z = 5$, 2.2 arcmin at $z = 10$, and 1.9 arcmin at $z = 20$. Due to computational limitations, our highest resolution images include 512^2 pixels. Thus, we are able to access multipoles from $l \sim 10^4$ to $l \sim 5 \times 10^6$.

Because our goal is to measure the degree of the non-gaussianity of the CMB maps, we need an appropriate tool for such a task. One of the most powerful mathematical tools to study different morphologies are Minkowski functionals.

2.2 Minkowski Functionals

Morphology, i.e. geometry and topology, of a random field can be quantified by a set of measures known as Minkowski functionals (Minkowski 1903). Although being known in mathematics since the beginning of 20th century, they were brought into cosmology not long ago by Mecke, Buchert & Wagner (1994) despite occasional partial rediscoveries (e.g. Gott et al. 1990). In the simplest form Minkowski functionals of a connected region represent three numbers characterizing the shape of a region: the area A , perimeter P , and genus G , which can be defined as $G = 1 - n_h$ where n_h is the number of holes in the region. Minkowski functionals are additive, therefore they have precise meaning for any set of the regions, and can be easily computed if they

are known for each region in the set. Minkowski functionals of the excursion set often called the global Minkowski functionals are particularly popular in cosmology (Gott et al. 1990; Schmalzing & Buchert 1997; Winitzki & Kosowsky 1997; Schmalzing & Górski 1998; Novikov, Feldman & Shandarin 1999; Novikov, Schmalzing & Mukhanov 2000; Wu et al. 2001; Shandarin et al. 2002). Global Minkowski functionals of the two-dimensional gaussian field is known analytically (Longuet-Higgins 1957)

$$\begin{aligned} A(u) &= \frac{1}{2} \left[1 - \operatorname{erf} \left(\frac{u}{\sqrt{2}\sigma} \right) \right], \\ P(u) &= \frac{1}{2R} \exp \left(-\frac{u^2}{2\sigma^2} \right), \\ G(u) &= \frac{1}{(2\pi)^{\frac{3}{2}}} \frac{1}{R^2} u \exp \left(-\frac{u^2}{2\sigma^2} \right), \end{aligned} \quad (1)$$

where $R = \sqrt{2}\sigma/\sigma_1$ is the scale of the field; σ and σ_1 are the rms of the field and its first derivatives (in statistically isotropic fields both derivatives $\partial u/\partial x$ and $\partial u/\partial y$ have equal rms). It is assumed that $\langle u \rangle = 0$. Here $A(u)$ is the fraction of the total area in the regions of the excursion set, $P(u)$ is the total length of the contour or total perimeter per characteristic area R^2 , and $G(u)$ is the (number of regions) - (number of holes) per R^2 .

The popularity of the global Minkowski functionals is probably related to the existence of the analytic formulae (eq. 1) and computational easiness. Computing global Minkowski functionals is usually done simply by identifying the pixels satisfying the threshold condition and applying the Crofton formulae (Crofton 1968). Unfortunately, this simple technique is quite crude resulting in nonconvergence of the contour length. For large maps a statistical correction can be applied (Winitzki & Kosowsky 1997), however its effects in finite size maps is not quantified. The least effect would be a significant growth of noise. We use a different technique which identifies every region in the excursion set and computes its area, perimeter and genus from the contour points obtained by the interpolation between pixels. One can find the details of the technique in (Shandarin et al. 2002). In addition to significant increase of the accuracy the method allows to use additional information about individual regions of the excursion set. In this study along with global Minkowski functionals we also use the number of regions (or - using the jargon of the cluster analysis - number of clusters N_{cl}) and the Minkowski functionals of the largest area region (A_p, P_p and G_p) labeled as percolating cluster since it plays a crucial role in identifying the percolating transition. The Minkowski functionals of the percolating cluster of gaussian fields are not known in analytic form but can be easily computed (see e.g. Shandarin (2002)). We parameterize the measurements by the total area in the excursion set A_g measured in units of the total area of the map. The advantages of this parameterization are described in Shandarin (2002).

Since Minkowski functionals depend on the power spectrum (R and σ are obviously determined by the power spectrum) of the statistical field, we need to separate this dependence from the dependence on the non-gaussian statistics. For this purpose for each simulated field of CMB anisotropies we produce 100 gaussian realizations with exactly the same power spectrum, and analyze these gaussian

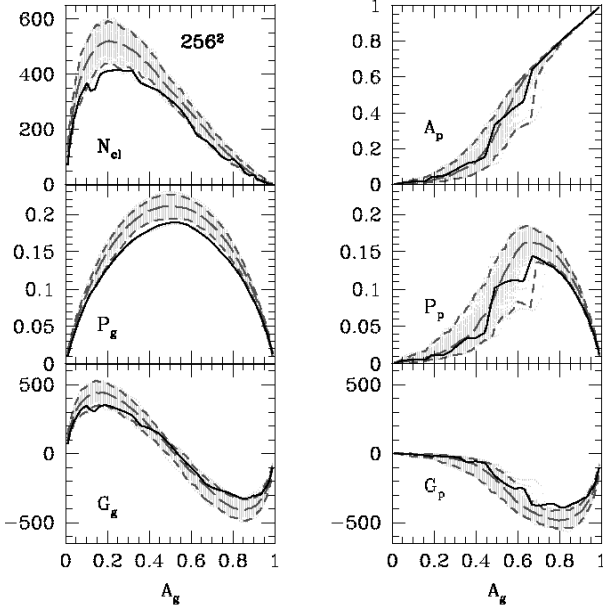


Figure 1. Five Minkowski functionals and the number of regions in the excursion set as a function of fractional area for the simulated data (black solid lines) and 100 gaussian realizations (light grey dotted lines) for a 256^2 image. Medium grey long and short dashed lines show the median and 95% probability interval for the set of gaussian curves.

realization in exactly the same manner as the simulated field. This also reduces the discreteness and boundary effects. We can then compare Minkowski functionals for the simulated image and for the gaussian realizations in order to measure the non-gaussian signal.

An example of such a comparison for all 6 functionals considered here is given in Figure 1. The behavior of all functionals is typical for all grids.

Plotting the deviation from the median of 100 gaussian realizations better illustrates the type of non-gaussianity in the $\Delta T/T$ fields (Figure 2). Generally there are fewer regions N_{cl} and the global perimeter P_g is shorter than in the corresponding gaussian fields. The global genus G_g at very small A_g (i.e. for rare peaks) is close to N_{cl} , since rare peaks have no holes. However, at the other extreme it is significantly affected by the presence of holes and is different from the gaussian genus. The area of the percolating region does not differ much from the gaussian fields but the perimeter of the percolating region generally somewhat shorter. The genus of the percolating region G_p shows more significant deviation from the gaussian field indicating that the number of holes in the largest region is smaller than in the gaussian case. Comparing it with the corresponding part of the global genus (at $A_g > 0.5$) one can see the influence of small regions: they are present in G_g but omitted in G_p .

One can notice that the number of clusters N_{cl} , the isocontour perimeter P_g and the genus G_p show the strongest deviations from the gaussian distribution. The global perimeter P_g is measured in the grid units and then normalized to one site.

In the rest of this paper we will focus on G_p and P_g functionals for brevity.

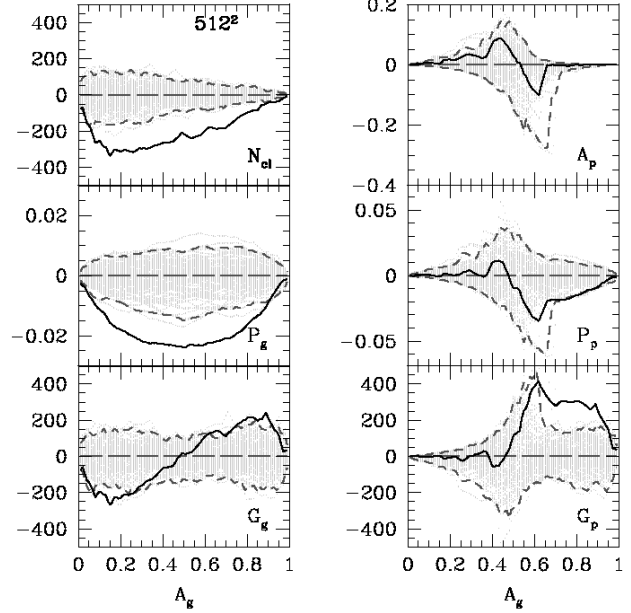


Figure 2. The deviations of the simulated data (black solid lines) from the median of 100 gaussian realizations (light grey dotted lines) for a 512^2 image. Medium grey short dashed lines show the 95% probability interval for the set of gaussian curves.

2.3 Measuring Non-gaussianity

The task of quantifying the degree of deviation of the simulation from the gaussian distribution is a formidable one and is generally an unsolved mathematical problem. Specifically, we would like to know how much gaussian or non-gaussian are the black curves in Fig. 1. Because we cannot solve this problem in a general case, we have designed the following simple approach that allows us to measure the degree of non-gaussianity in some cases and identify cases where this cannot be done.

We start by assuming that we can treat each curve $y(x)$ in the interval $0 < x < 1$ as a collection of random variables $y_j = y(x_j)$ where $x_j, j = 1..n$ is a subdivision of the interval $[0, 1]$ (it does not have to be uniform). We then treat y_j from gaussian realizations as gaussian random variables (this is the main assumption), so that the joined probability for all y_j for a given curve $y(x)$ is

$$p(y_j)d^n y = \exp \left[-\frac{1}{2} \sum_{i=0}^n \sum_{j=0}^n C_{ij}^{-1} (y_i - \bar{y}_i)(y_j - \bar{y}_j) \right],$$

where $\bar{y}_j \equiv \langle y_j \rangle$ is the mean for y_j and

$$C_{ij} \equiv \langle (y_i - \bar{y}_i)(y_j - \bar{y}_j) \rangle$$

is the correlation function. Both \bar{y}_j and C_{ij} can be computed directly from 100 gaussian realizations.

Then for a given collection of \hat{y}_j from the simulated map we can compute the “effective” chi-square

$$\chi_{\text{eff}}^2 \equiv \sum_{i=0}^n \sum_{j=0}^n C_{ij}^{-1} (\hat{y}_i - \bar{y}_i)(\hat{y}_j - \bar{y}_j). \quad (2)$$

The problem with this approach is that often C_{ij} is ill-defined if the curves are smooth and neighbouring points

y_j and y_{j+1} are highly correlated. In order to avoid small eigenvalues in matrix C_{ij} we use the Singular Value Decomposition to expand the correlation matrix as

$$C_{ij} = \sum_{k=0}^n U_{ik} w_k V_{jk},$$

where w_k are eigenvalues of C_{ij} and matrices U_{ik} and V_{jk} are orthonormal. We can then rewrite the effective chi-square (2) as a sum over inverse eigenvalues,

$$\chi_{\text{eff}}^2 = \sum_{i=0}^n \sum_{j=0}^n \sum_{k=0}^n \frac{1}{w_k} V_{ik} U_{jk} (\hat{y}_i - \bar{y}_i)(\hat{y}_j - \bar{y}_j). \quad (3)$$

Let us now consider not the full sum but a partial sum, where we assume that w_k are sorted in the descending order (they are all positive since the correlation matrix is always positive definite),

$$\chi_{\text{eff}}^2(l) = \sum_{i=0}^n \sum_{j=0}^n \sum_{k=0}^l \frac{1}{w_k} V_{ik} U_{jk} (\hat{y}_i - \bar{y}_i)(\hat{y}_j - \bar{y}_j). \quad (4)$$

The expression $q(l) \equiv \chi_{\text{eff}}^2(l)/l$ as a function of l reaches a maximum at some value of l_{max} . If we interpret $q(l)$ as chi-square per degree of freedom l , then l_{max} gives us the number of degrees of freedom present in the simulated curve \hat{y}_j , and we choose to truncate the sum (4) at this value of l - thus, discarding small w_k which makes the inverse correlation matrix ill-defined.

Because $q(l_{\text{max}})$ is not real chi-square, we cannot use standard tables to compute the confidence level on our simulated curve. Instead, we compute $q(l_{\text{max}})$ for 100 gaussian curves y_j and compare the cumulative distribution $P(> q)$ for 100 gaussian realization with the value \hat{q} for the simulation. If \hat{q} falls within the range of values that gaussian realizations span, we can directly estimate the probability that the simulation is non-gaussian by counting how many gaussian realizations have $q(l_{\text{max}})$ greater then \hat{q} . However, because we only have 100 gaussian realization, we cannot measure probabilities better than 1% in this way. So, if \hat{q} does not lie within the range spanned by gaussian realizations, we assume that $q(l_{\text{max}})$ for gaussian realizations indeed obey the chi-square distribution and compute the confidence level on \hat{q} from that assumption. We also compare the distribution of $q(l_{\text{max}})$ with the true chi-square distribution using the Kolmogorov-Smirnov test, and when this test fails our assumption becomes invalid. In that case we can only say that the simulation is non-gaussian at better than 99% confidence level.

3 RESULTS

Figure 3 shows the effect of angular resolution of the measurement of the Minkowski functionals. For brevity, we only show the genus of the percolating region as a function of total area of the excursion set for four values of angular resolution (which also implies different pixel sizes because the image size is fixed to 2.2 arcmin). In order to provide a better illustration we plot the deviation of the genus from the median value obtained from 100 gaussian realizations. As one can see, higher resolution gives progressively more non-gaussian signal.

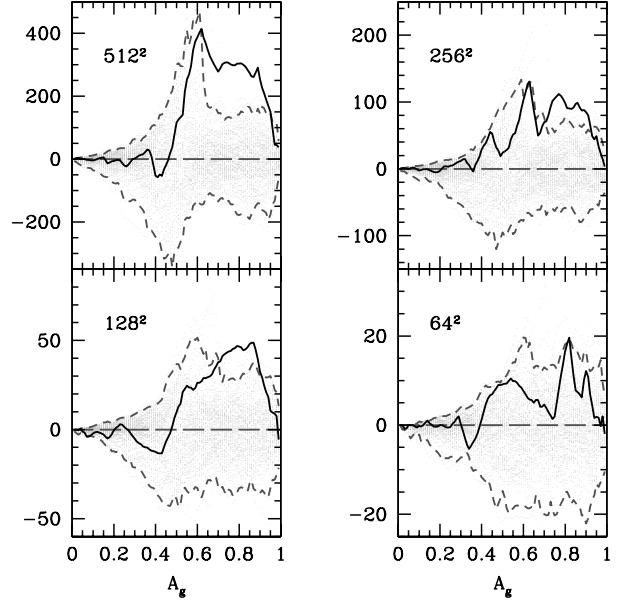


Figure 3. The deviation of the genus of the percolating region from the median value of 100 gaussian realizations as a function of the total area of the excursion set for four resolutions of the simulated image (64^2 - 2 arcsec pixel, 128^2 - 1 arcsec pixel, 256^2 - $1/2$ arcsec pixel, and 512^2 - $1/4$ arcsec pixel). Line markings are as in Fig. 1.

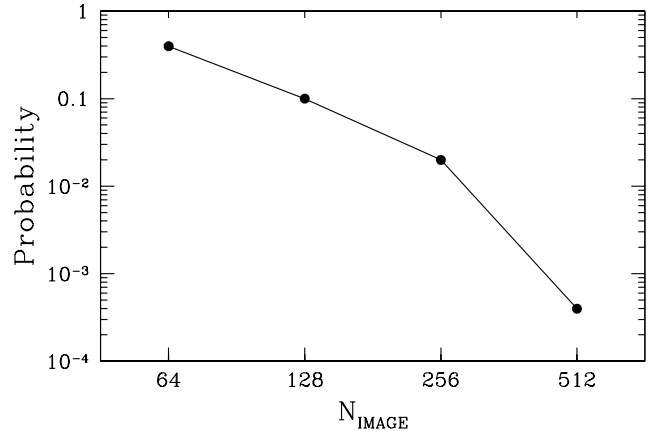
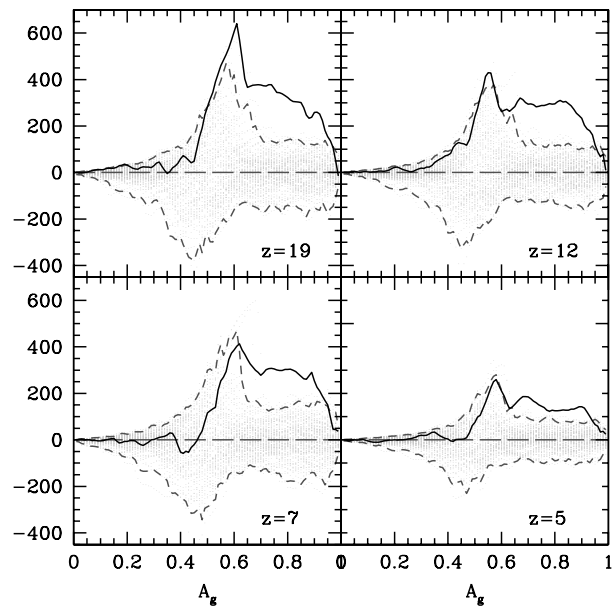


Figure 4. The probability that the simulation image is a gaussian realization as a function of resolution (i.e. the image size). Higher resolution images are more non-gaussian.

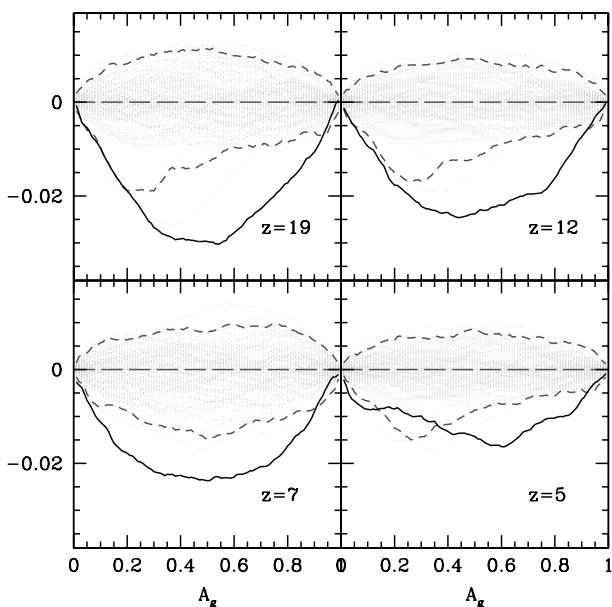
This is illustrated in Figure 4, which shows the probability that the signal is gaussian as a function of the image size. The number of clusters statistic N_{cl} and global perimeter P_g show similar trends.

This trend is easy to understand: as the resolution increases, we probe progressively smaller spatial scales that are more non-linear - and, thus, more non-gaussian - than larger scales.

A similar trend is observed when we change the redshift of reionization (we follow the specific procedure described in Gnedin & Jaffe (2001)). The redshift of reionization is defined as the moment at which the rate of change of the mean



(a)



(b)

Figure 5. (a) deviation from the median value of the genus of the percolating region and (b) deviation from the median value of the perimeter of the excursion set as a function of area for 512^2 resolution and four different epoch of reionization: $z = 5, 7, 12,$ and 19 . Line markings are as in Fig. 1.

free path to ionizing radiation peaks. It roughly corresponds to the moment when the volume weighted mean fraction of neutral hydrogen is about 10%.

Figure 5 shows the genus and perimeter, but other Minkowski functionals follow a similar trend. In this figure we again show the deviations from the median.

For this result to hold, however, it does not matter whether the universe is reionized completely or the neutral fraction remains of the order of 10% or so. After all, the

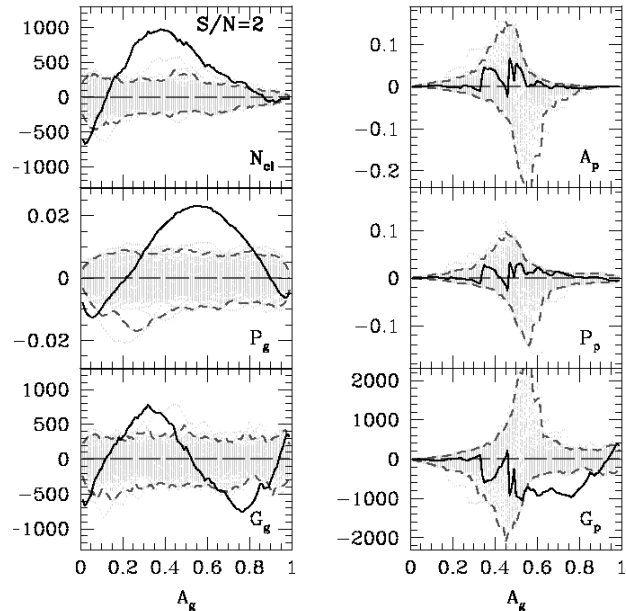


Figure 6. The deviations of the simulated data (black solid lines) from the median of 100 gaussian realizations (light grey dotted lines) for a 512^2 image with noise. $S/N = 2$ Medium grey short dashed lines show the 95% probability interval for the set of gaussian curves.

CMB anisotropies are sensitive to the total optical depth. So, if the mean neutral fraction drops to 10% at, say, $z \sim 20$, and the complete reionization (during which the neutral fraction drops to $10^{-4} - 10^{-5}$) takes place at $z \sim 6$, our results for $z = 20$ would apply, whereas neither radio observations (because the neutral fraction is only 10%) nor optical/IR observations (because the neutral fraction is still 10%) will be able to obtain any information about the “smoldering reionization” period from $z \sim 20$ to $z \sim 6$.

Real observations are almost always suffer from noise. In order to test the robustness of the morphological statistic used here, we added gaussian noise to the maps of the model with the reionization epoch at $z = 12$. Besides the model without noise we analyzed the models with the signal to noise ratios $S/N = 1/5, 1/4, 1/3, 1/2, 1, 2, 3.3, 5, 10, 20, 50$. We found that increasing noise from zero to about $S/N = 2$ the deviations of the Minkowski functionals from the median of the gaussian ensemble steadily change from that shown in fig.2 to fig.6. The further decrease of the signal to noise ratio between $S/N = 1/2$ and $S/N = 1/3$ eventually makes the non-gaussian signal undetectable as illustrated by fig.7. Quantitatively the probabilities of the number of regions N_{cl} shown in fig.7 to be gaussian are much less than 1% for $S/N = 2, 1$ and $1/2$ and is about 5% for $S/N = 1/3$. We remind that making comparison with only one hundred gaussian fields one cannot reliably estimate this probability much better than 1%.

This conclusion is also rather insensitive to the precise value of the neutral fraction during the “smoldering” phase. Really, for our values for the cosmological parameters, the Thompson optical depth accumulated from the redshift interval from z_1 to z_2 is

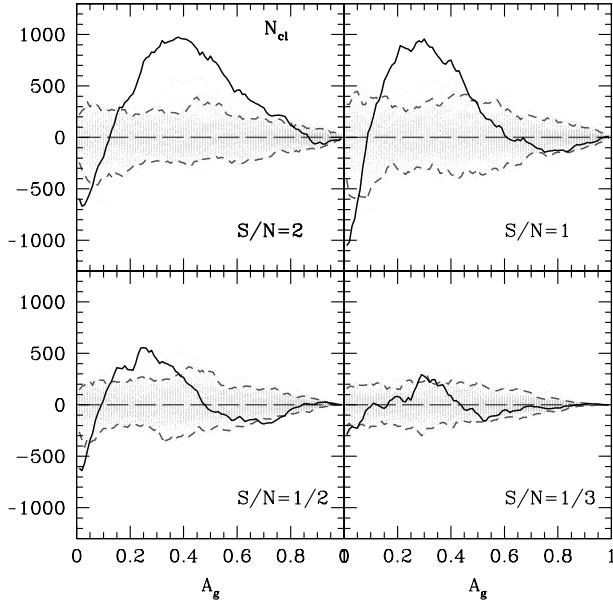


Figure 7. The deviations from the median value of the number of regions for a 512^2 image with different ratios of the signal to noise. Notations are as in fig 6

$$\begin{aligned} \tau(z_1, z_2) &= c\sigma_T \int_{t_1}^{t_2} n_e dt = \\ &= 2 \times 10^{-3} \left[(1+z_2)^{3/2} - (1+z_1)^{3/2} \right]. \end{aligned}$$

Thus, if we assume that the universe is fully reionized at $z = 6$, the interval from $z = 6$ to $z = 0$ produces $\tau(0, 6) = 0.035$. A period of “smoldering” reionization from $z = 20$ to $z = 6$ with the average free electron fraction x_e would give another contribution to the Thompson optical depth of $\tau(6, 20) = 0.16x_e$. For example a model in which the universe reionizes fully at $z = 12$ is very similar to the model which reionizes fully at $z = 6$ but has a period of “smoldering reionization” from $z = 20$ to $z = 6$ with $x_e = 0.35$.

Thus, until x_e drops below about $0.035/0.16 = 0.2$, it will be possible to detect the period of “smoldering” reionization. In that case, however, radio observations will likely be capable of tracing the neutral hydrogen abundance.

Of course, if the period of “smoldering” reionization is shorter, the sensitivity to the average free electron fraction will be respectively weaker. However, for the scenario proposed in Venkatesan et al. (2001), the effect is indeed measurable.

4 CONCLUSIONS

We showed how the morphological analysis of the maps of the secondary CMB anisotropies on sub-arcminute angular scales can detect an extended period of “smoldering” reionization, during which the universe remains partially ionized. If the neutral hydrogen fraction during such a period is below about 50% but still well above 10^{-5} , such a period will be detectable neither by radio observations of the redshifted 21cm line nor by IR observations of the Lyman-alpha forest.

In that case morphology of the CMB anisotropies offers the best chance to probe the IGM at early times.

We computed each of six parameters as a function of the fractional area of the excursion set, A_g : 1) the number of regions in the excursion set, N_{cl} , 2) total perimeter in the excursion set, P_g , 3) genus of the excursion set defined as the number of regions minus the number of holes, G_g , 4) area of the largest (i.e. percolating) region, A_p , 5) perimeter of the largest region, P_p , and 6) the genus of the largest region, G_p . Three parameters (A_g , P_g and G_g) are known as the global Minkowski functionals of the excursion set, and A_p , P_p and G_p are the Minkowski functionals of largest (by area) region. We found N_{cl} , P_g , and G_p are particularly sensitive to the non-gaussianity in $\Delta T/T$ maps due to secondary reionization, they are also the most robust to effects of noise. A_p and P_p are not sensitive to this type of non-gaussianity, G_g is significantly less sensitive than N_{cl} , P_g , and G_p . Using N_{cl} , P_g , and G_p one can detect the non-gaussianity in the CMB maps with $S/N = 1/2$ at the significance level of better than 99%.

Morphological analysis of the shapes of individual regions in the excursion set provides considerably more information about non-gaussianity of the maps and potentially may improve the current result both in terms of the resolution of the maps and signal to noise ratio. We reserve this study for the future work.

Acknowledgments: S.Sh. acknowledges the support of the GRF 2002 grant at the University of Kansas. This work was partially supported by National Computational Science Alliance under grant AST-960015N and utilized the SGI/CRAY Origin 2000 array at the National Center for Supercomputing Applications (NCSA).

REFERENCES

- Aghanim, N., Desert, F. X., Puget, J. L., Gispert, R. 1996, *A&A*, 311, 1
- Becker, R. H., et al. 2000, *AJ*, in press (astro-ph/0108097)
- Bruscoli, M., Ferrara, A., Fabbri, R., & Ciardi, B. 2000, *MNRAS*, 318, 1068
- Carilli, C. L., Gnedin, N. Y., Owen, F. 2002, *ApJ*, submitted (astro-ph/02....)
- Crofton, M.W., 1968, *Phil.Trans.Roy.Soc. London* 158, 181
- da Silva, A. C., Barbosa, D., Liddle, A. R., Thomas, P. A. 2000, *MNRAS*, 317, 37
- Djorgovski, S. G., Castro, S. M., Stern, D., Mahabal, A. 2001, *ApJL*, in press (astro-ph/0108069)
- Gnedin, N. Y. 2000, *ApJ*, 535, 530
- Gnedin, N. Y., Jaffe, A. H. 2001, *ApJ*, 551, 3
- Gott III J.R., Park C., Juszkiewicz R., Bies W.E. Bennett D.P., Bouchet R.R., & Stebbins A., 1990, *ApJ*, 352, 1
- Gruzinov, A., Hu, W. 1998, *ApJ*, 508, 435
- Haiman, Z., Knox, L. 1999, in *ASP Conf. Ser.* 181, *Microwave Foregrounds*, eds. A. de Oliveira-Costa & M. Tegmark (San Francisco: ASP), 227
- Hu, W. 2000, *ApJ*, 529, 12
- Hu, W., White, M. 1996, *A&A*, 315, 33
- Iliev, I. T., Shapiro, P. R., Ferrara, A., Martel, H. 2002, *ApJL*, submitted (astro-ph/0202410)
- Jaffe, A. H., Kamionkowski, M. 1998, *Phys. Rev. D*, 58, 043001
- Knox, L., Scoccimarro, R., & Dodelson, S. 1998, *Phys. Rev. Lett.*, 81, 2004
- Longuet-Higgins M.S., 1957, *Phil. Trans.Roy.Soc.London*, A, 249, 321

- Madau, P., Ferrara, A., Rees, M. J. 2001, ApJ, 555, 92
Madau, P., Meiksin, A., Rees, M. J. 1997, ApJ, 475, 429
Mecke K.R., Buchert T. & Wagner H., 1994, A&A, 288, 697
Minkowski H., 1903, Math. Ann., 57, 447
Novikov D.I., Feldman H. & Shandarin S.F., 1999, Int. J.Mod. Phys. D8, 291
Novikov D., Schmalzing J. & Mukhanov V.F., 2000, A&A, 364, 17
Oh, S. P. 2001, ApJ, 553, 499
Oh, S. P., Nollett, K. M., Madau, P., Wasserburg, G. J. 2001, ApJ, 562, L1
Peebles, P. J. E., Juskiewicz, R. 1998, ApJ, 509, 483
Refregier, A., Komatsu, E., Spergel, D. N., Pen, U.-L. 2000, Phys. Rev. D, 61, 3001
Seljak, U., Burwell, J., & Pen, U.-L. 2001, Phys. Rev. D, 63, 3001
Schmalzing J. & Buchert T., 1997, ApJ, 482, L1
Schmalzing J. & Górski K.M., 1998, MNRAS, 297, 355
Shandarin S.F., 2002, MNRAS, 331, 865
Shandarin S.F., Feldman H.A., Xu Y., & Tegmark M., 2002, ApJS, 141 (astro-ph/0107136)
Springel, V., White, M., & Hernquist, L. 2001, ApJ, 549, 681
Steidel, C. C., Adelberger, K. L., Ciavallisco, M., Dickinson, M., Pettini, M. 1999, ApJ, 519, 1
Tozzi, P., Madau, P., Meiksin, A., Rees, M. J. 2000, ApJ, 528, 597
Venkatesan, A., Giroux, M. L., Shull, J. M. 2001, ApJ, 563, 1
Winitzki S. & Kosowsky A., 1997, New Astronomy, 3, 75
Wu J-H. P., Babul A., Borrill J., Ferreira P.G., Hanany S., Jaffe A.H. Lee A.T., Rabii B., Richards P.L., Smoot G.F., Stompor R., & Winant C.D., 2001, Phys. Rev.Lett. 87, 251303